

JAAS

Accepted Manuscript



This is an *Accepted Manuscript*, which has been through the Royal Society of Chemistry peer review process and has been accepted for publication.

Accepted Manuscripts are published online shortly after acceptance, before technical editing, formatting and proof reading. Using this free service, authors can make their results available to the community, in citable form, before we publish the edited article. We will replace this *Accepted Manuscript* with the edited and formatted *Advance Article* as soon as it is available.

You can find more information about *Accepted Manuscripts* in the [Information for Authors](#).

Please note that technical editing may introduce minor changes to the text and/or graphics, which may alter content. The journal's standard [Terms & Conditions](#) and the [Ethical guidelines](#) still apply. In no event shall the Royal Society of Chemistry be held responsible for any errors or omissions in this *Accepted Manuscript* or any consequences arising from the use of any information it contains.

1
2
3
4 1 **Elemental fractionation during condensation of plasma**
5
6 2 **plumes generated by laser ablation: a ToF-SIMS study of**
7
8
9
10 3 **condensate blankets**
11
12
13 4

15 5 Ming Tang^{a,*}, Ricardo Arevalo Jr.^b, Yulia Goreva^c, William F. McDonough^a
16
17 6

20 7 ^a*Department of Geology, University of Maryland, College Park, Maryland 20742, USA*
21

22 8 ^b*NASA Goddard Space Flight Center, Greenbelt, Maryland 20771, USA*
23

24 9 ^c*Smithsonian Institution, Washington, DC 20013-7012, USA*
25
26
27 10
28
29 11

31 12 **Abstract**
32
33
34 13

35
36
37 14 Ion imaging of the condensate blanket around a laser ablation site provides a window to
38
39 15 study elemental fractionation during condensation of a plasma plume. Here we used a
40
41 16 Time-of-Flight Secondary Ion Mass Spectrometer (ToF-SIMS) to conduct depth profiling
42
43 17 of the condensate blanket produced by excimer 193 nm laser ablation of NIST 610 glass.
44
45 18 Compositional zonings (Ca normalized) revealed by ToF-SIMS are associated with
46
47 19 texture gradients in the condensate blanket, as characterized by Secondary Electron
48
49
50

51
52
53 * Corresponding author at: *Department of Geology, University of Maryland, College Park,*
54 *Maryland 20742, USA. Tel.: +1 2403743443; fax: +1 (301) 405-3597.*

55
56 *E-mail: tangmyes@gmail.com (Ming Tang).*
57
58
59
60

1
2
3 20 Microprobe (SEM) images. Elements that are more volatile than Ca are relatively
4
5 21 enriched in the inner zones (proximal to the ablation site) while more refractory elements
6
7
8 22 are variable in their distributions. Volatility and ionization potential exert influence on
9
10 23 elemental fractionation in plasma plume condensation processes as documented by the
11
12 24 contrasting fractionation behaviors of alkaline and alkaline earth metals. Compositional
13
14 25 zonings in the condensate blanket are due to physical and chemical zonings (e.g.,
15
16 26 temperature, pressure, electron density, speciation, etc.) within the condensing plume as it
17
18 27 expands and cools. Zoned condensation may be a primary mechanism driving the
19
20 28 elemental fractionation associated with laser ablation.
21
22
23
24
25
26
27
28

29
30
31

31 Introduction

32 Elemental and isotopic fractionations have been documented for laser ablation (LA) of
33 various materials¹ and the references therein. Progressive localized ablation, leading to deeper
34 incision of the sample substrate, exacerbates laser-induced fractionation and serves as one
35 of the largest contributions to the uncertainty budget when characterizing the products of
36 laser ablation - inductively coupled plasma - mass spectrometry (LA-ICP-MS). Chemical
37 and isotopic fractionation during plasma condensation and particle formation should not
38 be underestimated. Understanding these fractionation mechanisms is key to achieving
39 high accuracy and precision in quantitative analysis using laser micro-sampling
40 techniques such as LA-ICP-MS.

41 Laser processing of geological materials (insulators to conductors) involves
42 photochemical and photothermal activation², which are primarily controlled by the pulse

1
2
3
4
5
6
7
8
9
10
11
12
13
14
15
16
17
18
19
20
21
22
23
24
25
26
27
28
29
30
31
32
33
34
35
36
37
38
39
40
41
42
43
44
45
46
47
48
49
50
51
52
53
54
55
56
57
58
59
60

1
2
3 43 irradiance duration of the incident laser light. Specifically, lasers with nanosecond pulse
4
5 44 durations (the vast majority of commercial laser ablation systems) remove materials via
6
7
8 45 inducing electronic transitions attended by significant melting and evaporation², as most
9
10 46 rocks and minerals are defined by phonon relaxation rates on the order of 10^{-12} s (e.g.,
11
12 47 Bauerle, 1996). In addition to pulse duration, the ablation mechanisms are also controlled
13
14 48 by laser wavelength^{3, 4} and fluence^{2, 5, 6}. Elements with different physical (e.g., volatility)
15
16 49 and chemical (e.g., electronic structure) affinities fractionate significantly during laser-
17
18 50 matter interaction and plasma condensation^{4, 7-11}. Laser-induced elemental fractionation
19
20 51 results in non-stoichiometric composition of the aerosol, which scales critically on
21
22 52 particle size distributions^{8, 12-15}. Such elemental fractionation is further aggravated during
23
24 53 aerosol transportation (particle loss) and ionization (incomplete ionization) of large
25
26 54 particles ($> \sim 1 \mu\text{m}$) in the ICP^{9, 13, 16, 17}. Non-stoichiometric compositions of ablated
27
28 55 aerosols are at least partially generated from particle formation processes, of which
29
30 56 plasma-to-particle conversion plays an important role. Plasma-to-particle conversion
31
32 57 progresses from nucleation to condensation coalescence and agglomeration within the
33
34 58 expanding plume¹⁸. These particles ultimately form a condensate blanket near the
35
36 59 ablation site if not extracted by carrier gas.

37
38
39 60 Here we present a Time-of-Flight Secondary Ion Mass Spectrometry (ToF-SIMS) study
40
41 61 of the condensate blanket produced by laser ablation of NIST 610 glass with nanosecond
42
43 62 pulses of 193 nm wavelength laser radiation. ToF-SIMS is a surface-sensitive technique
44
45 63 that uses a pulsed primary ion beam and images only the outmost ($n = 1 - 2$) atomic
46
47 64 layers of the surface analyzed. Elements and a wide range of molecular species can be
48
49 65 detected, though there is a wide range of sensitivities among the elements based on their
50
51
52
53
54
55
56
57
58
59
60

1
2
3 66 first ionization potentials¹⁹. Ion imaging of laser condensate blankets represents a
4
5
6 67 snapshot of the compositional variation within the laser induced plume, and provides key
7
8 68 information for characterizing elemental fractionation during particle formation
9
10 69 processes.
11

12
13 70

14 15 71 **Experimental**

16 17 18 72 **Laser ablation**

19
20 73 A freshly polished section of the standard reference material NIST 610 (~400 parts per
21
22 74 million by weight concentrations of most trace elements. Detailed compositional data are
23
24 75 available at GeoReM: http://georem.mpch-mainz.gwdg.de/sample_query_pref.asp) was
25
26 76 irradiated by a Photon Machines Analyte G2 excimer (ArF) laser ablation system at
27
28 77 NASA Goddard Space Flight Center. This laser produces 193 nm wavelength radiation in
29
30 78 4 ns pulses at repetition rates up to 100 Hz. For this study, a laser spot with the following
31
32 79 parameters was processed on the reference material:
33
34
35

36
37 80 110 μm spot diameter, 10 Hz repetition rate, 2.0 J/cm^2 fluence, and 500 total shots.

38
39 81 Prior to irradiation, the sample chamber (Helix cell) was purged with a He gas flow up to
40
41 82 2 L/min in order to evacuate any particulate contamination. During sample processing,
42
43 83 however, the flow of helium was disengaged (i.e., 0 L/min He) and the reference material
44
45 84 was ablated under a static He atmosphere.
46
47

48
49 85

50 51 86 **Secondary Electron Microprobe (SEM) imaging**

52
53 87 Backscattered Electron (BSE) imaging and Energy Dispersive Spectrometry (EDS)
54
55 88 analysis were performed using a 7 kV electron beam with a 4.5 micron diameter and
56
57
58
59
60

1
2
3 89 gaseous analytical detector (GAD) on the FEI Nova nanoSEM 600 instrument at the
4
5 90 Smithsonian Institution. Low vacuum (1 mbar water vapor pressure) conditions allowed
6
7
8 91 imaging and analysis of glass samples that were not conductively coated.
9

10 92

13 **ToF-SIMS**

14
15 94 Ion imaging and depth profiling were performed using the ION TOF GmbH IV TOF-
16
17 95 SIMS instrument at the Smithsonian Institution. A primary 25 keV Bi⁺ beam (pulsed
18
19
20 96 current of 0.3 pA) was rastered over an area of 250 × 250 μm for 6000 seconds,
21
22 97 producing 600 consecutive each scans with ~ 2 μm/pixel lateral resolution. To improve
23
24
25 98 counting statistics we integrated every 40 scans to make an integrated scan, thus 15
26
27 99 integrated scans in total were made. Each integrated scan has a sputtering depth of ~3 nm
28
29
30 100 for a total penetration depth of ~48 nm for the 6000 s scanning. This sputtering rate was
31
32 101 estimated based on the sputtering rate obtained on silica glass, which is ~0.02 Å/s for a
33
34 102 500 × 500 μm² area.
35

36 103

37 104

42 **Results and discussion**

43
44 106 A distinct condensation blanket ~ 300 μm in diameter around the 110 μm laser crater is
45
46 107 apparent in BSE images (Fig. 1A). The surface texture varies across the condensation
47
48
49 108 blanket. The laser crater is surrounded by a narrow belt of beads that are 100 nm to 1 μm
50
51 109 in diameter (Fig. 1B, Zone 1). Farther from the ablation site (Zones 2 – 6), more fiber-
52
53 110 like condensates can be seen extending towards the boundary of inner zoning at 200 μm
54
55
56 111 from the crater (top of Zone 6); individual particles cannot be resolved in this “fiber”
57
58
59
60

1
2
3 112 zone. On the edge of the boundary (e.g., Fig 1C, Zones 5 – 7) are particle agglomerates of
4
5 113 $10^2 - 10^3$ nm, which show a clear preferred orientation. The surface area in the outer zone
6
7
8 114 appears to be filled with smaller (< 10 nm) condensates (e.g., Zones 8 – 9). The BSE
9
10 115 images also reveal massive particle agglomerates (up to $10 \mu\text{m}$) scattered throughout the
11
12 116 surface covering both the laser pit ejecta blankets and remote areas of the sample (all
13
14 117 Zones). These agglomerates have a similar composition as NIST 610 glass based on
15
16 118 EDS spectra, and thus were likely generated during laser ablation processing. For
17
18 119 comparison, we provide a “control” SEM image of an area far (~ 5 mm away from the
19
20 120 ablation site) from the laser crater (Fig. 2).
21
22
23
24
25
26

27 122 We used a ToF-SIMS instrument to produce ion images of an area that included
28
29 123 representative regions of the two distinct zones of condensation blanket (Fig. 1, panel A).
30
31 124 For ToF-SIMS data, we normalized all isotopes to ^{40}Ca ; the less abundant ^{43}Ca is
32
33 125 routinely used as an internal standard in LA-ICP-MS data reduction. It’s worth noting
34
35 126 that the X/Ca intensity ratios measured by ToF-SIMS do not reflect the accurate atomic
36
37 127 ratios in the blanket. Calcium and other metals fractionate during sputtering due to
38
39 128 different X-O bonding energies²⁰⁻²². For our purpose, we focused on the relative X/Ca
40
41 129 variation across the condensate blanket. Thus no external standard calibration was
42
43 130 applied. Examples of the distributions of X/Ca ratios (X is an element other than Ca) in
44
45 131 the first integrated scan are plotted in Fig. 3 (a complete set of integrated scans 2–15 are
46
47 132 available in the Electronic Supporting Information, *ESI*). Similar to the textural variation
48
49 133 across the condensate region, as revealed through BSE images, the ToF-SIMS images
50
51 134 show compositional zonings (Fig. 3). For ^7Li , ^9Be , ^{11}B , ^{48}Ti , ^{51}V , ^{55}Mn , ^{56}Fe , ^{58}Ni , ^{65}Cu ,
52
53
54
55
56
57
58
59
60

1
2
3 135 ^{69}Ga , ^{87}Rb and ^{133}Cs , the inner zones are demarked by higher $X/^{40}\text{Ca}$ intensity ratios; for
4
5 136 ^{27}Al , ^{88}Sr and ^{138}Ba , the outer zones have higher X/Ca intensity ratios. ^{26}Mg shows less
6
7
8 137 apparent fractionation across the frame. Sodium and potassium were also imaged by ToF-
9
10 138 SIMS; however, both Na and K are major surface contaminants. In addition, Na
11
12 139 oversaturated the detector. Therefore, Na and K data are not discussed here.
13
14
15 140 There are primarily two factors that may result in X/Ca variation: (1) laser induced
16
17 141 elemental fractionation; and (2) topography induced matrix effects during ToF-SIMS
18
19 142 analysis. The latter is a result of non-equilibrium sputtering. Generally, pre-sputtering can
20
21 143 destroy surface structure and remove surface contaminants so as to avoid non-equilibrium
22
23 144 sputtering effects. However, the non-equilibrium sputtering depth range is both matrix-
24
25 145 and element-dependent. In this study, we did not apply pre-sputtering, but used the depth
26
27 146 profiles to evaluate the non-equilibrium sputtering effect for each element. Relative
28
29 147 differences (in %) in average X/Ca between the outer zone (farthest 100 μm from the
30
31 148 ablation site) and inner zone (100 μm nearest the ablation site) for each integrated scan,
32
33 149 as a function of sputtering depth (integrated scan number), are calculated in Fig. 4 and
34
35 150 ESI. If disproportionate enrichments or depletions in elemental abundances revealed by
36
37 151 ToF-SIMS are solely due to topography changes across the condensation blanket, the
38
39 152 normalized X/Ca zoning trends shown in these figures (i.e., $X/\text{Ca}_{\text{outer}}/X\text{Ca}_{\text{inner}}$) should
40
41 153 “flatten out” with depth, as continuous sputtering is expected to resurface the sample and
42
43 154 approach equilibrium sputtering conditions. Consequently, it is unlikely that our depth
44
45 155 profiling penetrated through the condensate blanket, since the boundary between the
46
47 156 inner and outer zoning neither disappeared nor changed its position in the ToF-SIMS
48
49
50
51
52
53
54
55
56
57
58
59
60

1
2
3 157 images throughout the depth profile. Therefore our depth profile, sample the condensate
4
5
6 158 blanket and should reflect the plume composition at the late stage of the ablation.
7
8
9 159
10
11 160 Among the geochemical proxies investigated here, Mg/Ca, Cs/Ca and Al/Ca may have
12
13 161 non-equilibrium sputtering effects during early sputtering. For Mg, the Mg/Ca diff%
14
15 162 between the outer and inner zonings continuously decreases with depth and reaches a
16
17 163 plateau with a diff% of ~0% (Fig. 4), which suggests little Mg-Ca fractionation across the
18
19
20 164 condensation blanket. For Cs, Cs/Ca in the outer zoning continuously decreases with
21
22 165 sputtering depth while Cs/Ca in the inner zoning stays constant (Fig. 4), resulting in an
23
24 166 increasing Cs/Ca diff% from integrated scan #1-5 followed by a plateau with a diff% of
25
26 167 ~125%, indicating significant Cs-Ca fractionation induced by laser ablation. Al/Ca in the
27
28 168 inner and outer zonings evolve in the opposite directions with no diff% plateau reached
29
30 169 throughout the depth profile (Fig. 4); because of this, the fractionation between Al-Ca
31
32 170 observed here likely represents only a lower bound on the actual fractionation between
33
34 171 these elements. Although poorly resolved, Si/Ca and Cr/Ca appear to show decreased
35
36 172 diff% between the outer and inner zones with sputtering depth. For the remainder, X/Ca
37
38 173 diff% are significantly different from 0% with no resolvable systematic changes with
39
40 174 sputtering depth, reflecting reproducible X-Ca fractionation of various sizes across the
41
42 175 condensation blanket (see the ESI for depth profiles of all elements analyzed here).
43
44
45
46
47
48 176
49
50 177 Laser induced elemental fractionation has been attributed to different chemical and
51
52 178 physical properties of elements e.g., volatility^{5-7, 10, 23}, electronic structure^{6, 11}, etc.,
53
54
55 179 resulting in preferential evaporation, ionization and condensation during laser ablation
56
57
58
59
60

1
2
3 180 processes. Figure 5 shows that volatile and transitional elements (Ni to Cs, 50%
4
5 181 condensation temperature < 1360 K) are mostly enriched in the inner zone while
6
7 182 elements that are similarly refractory as Ca (V to Al, 50% condensation temperature >
8
9 183 1360 K) can be enriched in either outer or inner zones, reflecting multiple factors
10
11 184 controlling elemental fractionation. Multiple fractionation mechanisms can be further
12
13 185 elucidated by comparing the contrasting fractionation directions between alkaline metals
14
15 186 and alkaline earth metals (Fig. 6). Alkaline metals (Period IA elements) are volatile and
16
17 187 increasingly so with increasing atomic mass²⁴, with the enrichment in alkaline metals
18
19 188 increasing from Li to Cs in the inner zone (Figure 6a). Alkaline earth metals (Period IIA
20
21 189 elements), however, share similar volatilities but transition from relative enrichments to
22
23 190 progressive depletions in between the inner zone as a function of first ionization potential
24
25 191 (Fig. 6b), reflecting the control of electronic structure on the fractionation between
26
27 192 alkaline earth metals. The opposite fractionation directions between alkaline metals and
28
29 193 alkaline earth metals suggests the dominance of volatility effect over electronic structure
30
31 194 effect on laser induced elemental fractionation (LIEF). The volatility control may also be
32
33 195 responsible for the distinct fractionation behavior of Al compared with B and Ga since Al
34
35 196 is enriched in the outer zoning while the more volatile B and Ga are both enriched in the
36
37 197 inner zone (Fig. 4).
38
39
40
41
42
43
44
45
46
47

48 199 The compositional zonings around the laser crater are likely related to condensation
49
50 200 behaviors and the spatial – temporal evolution of particle formation and deposition
51
52 201 processes. Dynamically, during plasma plume initiation (10^{-10} s post-irradiation) the
53
54 202 ascending material also undergoes laser-induced ionization at the sample surface during
55
56
57
58
59
60

1
2
3 203 active irradiation with nanosecond (or longer) laser pulses²⁵⁻²⁷. Photothermally and
4
5 204 photochemically activated materials irradiated with $\sim 10^9$ W/cm² (i.e., ~ 2 J/cm², 4 ns, and
6
7
8 205 193 nm λ) rise from the sample surface and form a plasma plume, which in turn interacts
9
10 206 with the incident laser irradiation and absorbs significant amounts (circa $\geq 50\%$) of laser
11
12 207 energy that would otherwise couple with the sample, known as the plasma shielding
13
14
15 208 effect^{2, 28}. The absorption of incident photons results in elevated temperatures (up to 10^4
16
17 209 K) and electron densities in the plume. During plume expansion, the temperature drops
18
19 210 down and the excited species condense, aggregate and (eventually) form mostly sub-
20
21 211 micron- and micron-sized particles. Within the expanding plume, temperature, pressure,
22
23 212 electron density, and speciation (e.g., ionization degree) are zoned^{25-27, 29}. Moreover, for
24
25 213 plume residences time of 1 millisecond or longer, material in the pulse path will absorb
26
27 214 the next incoming light pulse at 100 Hz repetition rates. As a result, the temporal and
28
29 215 spatial scale condensation properties are expected to form condensates that
30
31
32 216 compositionally vary as a function of distance from the ablation center. Although
33
34 217 specifically developed for laser ablation of metallic substrates, Bogaerts and Chen's
35
36 218 models^{26, 27} show that the spatial distribution of temperatures within the expanding plume
37
38 219 is complex, and the plume develops a low temperature center after the laser pulse
39
40
41 220 terminates. This may explain the relative enrichments of many volatile elements (e.g.,
42
43 221 alkaline earth metals, B, etc.) in the inner zone of the condensation blanket. With
44
45 222 condensation being the primary stage of particle formation (as opposed to less dominant
46
47 223 evaporation processes, not discussed here), elemental fractionation during condensation
48
49 224 corroborates the linkage between LIEF and particle size distribution.
50
51
52
53
54
55
56
57
58
59
60

1
2
3 226 Because elemental fractionation happens during laser plume condensation, achieving
4
5 227 high accuracy and precision LA-ICP-MS data requires either complete mass transport
6
7
8 228 and ionization in the ICP, or well matched internal standard element that fractionates in
9
10 229 the same way as the unknown element during laser ablation of both the external standard
11
12 230 and sample^{11,30}. The former option requires well-designed laser ablation chamber and
13
14 231 small aerosol particles produced by laser ablation; the latter option requires dedicated
15
16 232 analysis of only a limited range of elements with similar physicochemical properties
17
18 233 (such as condensation temperature and first ionization potential) of the internal standard.
19
20
21 234
22
23
24 235 Finally, the findings of this study need to be placed into the context of active ablation
25
26 236 with a He gas stream of 2 L/min, typical of modern laser ablation sampling for chemical
27
28 237 and/or isotopic analyses. Under these conditions additional affects need to be considered,
29
30 238 given plume trajectories of 10^4 m s⁻¹ and strong gas flow velocities. Fractionation of
31
32 239 volatile/refractory element species is likely to be enhanced, particularly for highly
33
34 240 volatile elements Zn, Tl, Pb, In, Bi, Br and I. Horn et al (2000)³¹ observed correlation
35
36 241 between element fractionation (U/Pb) and spot geometry (their Figure 7) and suggested
37
38 242 that the laser-induced elemental fractionation also reflected the relative efficiency of
39
40 243 element transport for volatile versus refractory elements from the site of ablation to the
41
42 244 ICP-MS.
43
44
45
46
47
48 245
49
50 246
51
52

53 247 Conclusions

54
55
56
57
58
59
60

- 1
2
3 248 (1) ToF-SIMS imaging reveals compositional zoning in the condensate blanket
4
5 249 produced by ablation of NIST 610 glass with a pulsed (4 ns) ArF excimer (193
6
7
8 250 nm) laser system.
9
10 251 (2) The observed elemental fractionation is controlled by volatility as well as
11
12 252 electronic structure (ionization potential), with volatility being the more
13
14 253 influential factor; volatile and transitional elements (50% condensation
15
16 254 temperature < 1360 K) tend to be enriched in the inner zone relative to refractory
17
18 255 elements, and low first ionization potential elements tend to be enriched in the
19
20 256 inner zone relative to high first ionization potential elements.
21
22 257 (3) The elemental fractionation is associated with condensation and subsequent
23
24 258 particle formation processes, during which the gradients in physical and chemical
25
26 259 conditions result in uneven condensation within the plasma plume.
27
28 260 (4) ToF-SIMS imaging of laser condensate blanket provides a new approach to study
29
30 261 the mechanisms of laser induced elemental and isotopic fractionation.
31
32
33
34
35
36
37
38

39 Acknowledgements

40
41 264 This project is funded by NSF grants EAR-0739006 and EAR-0948549. The first author
42
43 265 also appreciates the support from the graduate school of the University of Maryland (Ann
44
45 266 G. Wylie Fellowship). ToF-SIMS work (Yulia Goreva) was supported by NASA grant
46
47 267 NNX14AF27G and funding from Deep Carbon Observatory. We thank editor Harriet
48
49 268 Brewerton for handling our paper, and two anonymous reviewers for their comments and
50
51 269 suggestions.
52
53
54
55
56
57
58
59
60

271 References

- 272 1. R. Arevalo Jr, in *Treatise on Geochemistry (Second Edition)*, ed. H. D. H. K.
273 Turekian, Elsevier, Oxford, 2014, DOI: [http://dx.doi.org/10.1016/B978-0-08-](http://dx.doi.org/10.1016/B978-0-08-095975-7.01432-7)
274 [095975-7.01432-7](http://dx.doi.org/10.1016/B978-0-08-095975-7.01432-7), pp. 425-441.
- 275 2. D. W. Bäuerle, *Laser Processing and Chemistry*, Springer, 2011.
- 276 3. M. Guillong, I. Horn and D. Gunther, *Journal of Analytical Atomic Spectrometry*,
277 2003, **18**, 1224-1230.
- 278 4. I. Horn, M. Guillong and D. Günther, *Applied Surface Science*, 2001, **182**, 91-
279 102.
- 280 5. X. Mao, W.-T. Chan, M. Caetano, M. A. Shannon and R. E. Russo, *Applied*
281 *Surface Science*, 1996, **96–98**, 126-130.
- 282 6. X. L. Mao, O. V. Borisov and R. E. Russo, *Spectrochimica Acta Part B: Atomic*
283 *Spectroscopy*, 1998, **53**, 731-739.
- 284 7. S. M. Eggins, L. P. J. Kinsley and J. M. G. Shelley, *Applied Surface Science*,
285 1998, **127–129**, 278-286.
- 286 8. J. Kosler, M. Wiedenbeck, R. Wirth, J. Hovorka, P. Sylvester and J. Mikova,
287 *Journal of Analytical Atomic Spectrometry*, 2005, **20**, 402-409.
- 288 9. I. Kroslakova and D. Gunther, *Journal of Analytical Atomic Spectrometry*, 2007,
289 **22**, 51-62.
- 290 10. M. Tang, W. F. McDonough and R. J. Arevalo, *Journal of Analytical Atomic*
291 *Spectrometry*, 2014, **29**, 1835-1843.
- 292 11. F. E. Jenner and H. S. C. O'Neill, *Geochemistry, Geophysics, Geosystems*, 2012,
293 **13**, Q03003.

- 1
2
3 294 12. J. Koch, A. von Bohlen, R. Hergenroder and K. Niemax, *Journal of Analytical*
4
5 295 *Atomic Spectrometry*, 2004, **19**, 267-272.
6
7
8 296 13. M. Guillong and D. Gunther, *Journal of Analytical Atomic Spectrometry*, 2002,
9
10 297 **17**, 831-837.
11
12 298 14. H.-R. Kuhn and D. Günther, *Analytical chemistry*, 2003, **75**, 747-753.
13
14 299 15. J. Mikova, J. Kosler, H. P. Longerich, M. Wiedenbeck and J. M. Hanchar,
15
16 300 *Journal of Analytical Atomic Spectrometry*, 2009, **24**, 1244-1252.
17
18 301 16. M. Guillong, H.-R. Kuhn and D. Günther, *Spectrochimica Acta Part B: Atomic*
19
20 302 *Spectroscopy*, 2003, **58**, 211-220.
21
22 303 17. S. H. Jeong, O. V. Borisov, J. H. Yoo, X. L. Mao and R. E. Russo, *Analytical*
23
24 304 *Chemistry*, 1999, **71**, 5123-5130.
25
26 305 18. R. Hergenroder, *Journal of Analytical Atomic Spectrometry*, 2006, **21**, 517-524.
27
28 306 19. T. Stephan, *Planetary and Space Science*, 2001, **49**, 859-906.
29
30 307 20. T. Henkel and J. Gilmour, in *Treatise on Geochemistry (Second Edition)*, ed. H.
31
32 308 D. H. K. Turekian, Elsevier, Oxford, 2014, DOI: [http://dx.doi.org/10.1016/B978-](http://dx.doi.org/10.1016/B978-0-08-095975-7.01431-5)
33
34 309 [0-08-095975-7.01431-5](http://dx.doi.org/10.1016/B978-0-08-095975-7.01431-5), pp. 411-424.
35
36 310 21. T. R. Ireland, in *Treatise on Geochemistry (Second Edition)*, ed. H. D. H. K.
37
38 311 Turekian, Elsevier, Oxford, 2014, DOI: [http://dx.doi.org/10.1016/B978-0-08-](http://dx.doi.org/10.1016/B978-0-08-095975-7.01430-3)
39
40 312 [095975-7.01430-3](http://dx.doi.org/10.1016/B978-0-08-095975-7.01430-3), pp. 385-409.
41
42 313 22. J. C. Vickerman, J. C. V. D. Briggs and D. Briggs, *ToF-SIMS: Materials Analysis*
43
44 314 *by Mass Spectrometry*, IM Publications, 2013.
45
46 315 23. C. Liu, X. L. Mao, S. S. Mao, X. Zeng, R. Greif and R. E. Russo, *Analytical*
47
48 316 *Chemistry*, 2003, **76**, 379-383.
49
50
51
52
53
54
55
56
57
58
59
60

- 1
2
3 317 24. K. Lodders, *The Astrophysical journal*, 2003, **591**, 1220.
4
5 318 25. A. Bogaerts and Z. Chen, *Journal of Analytical Atomic Spectrometry*, 2004, **19**,
6
7 319 1169-1176.
8
9 320 26. A. Bogaerts and Z. Chen, *Spectrochimica Acta Part B: Atomic Spectroscopy*,
10
11 321 2005, **60**, 1280-1307.
12
13 322 27. Z. Chen and A. Bogaerts, *Journal of Applied Physics*, 2005, **97**, 063305.
14
15 323 28. R. E. Russo, X. Mao, H. Liu, J. Gonzalez and S. S. Mao, *Talanta*, 2002, **57**, 425-
16
17 324 451.
18
19 325 29. A. Bogaerts, Z. Chen, R. Gijbels and A. Vertes, *Spectrochimica Acta Part B:*
20
21 326 *Atomic Spectroscopy*, 2003, **58**, 1867-1893.
22
23 327 30. M. Gaboardi and M. Humayun, *Journal of Analytical Atomic Spectrometry*, 2009,
24
25 328 **24**, 1188-1197.
26
27 329 31. I. Horn, R. L. Rudnick and W. F. McDonough, *Chemical Geology*, 2000, **164**,
28
29 330 281-301.
30
31 331
32
33 332
34
35 333

334 **Figure captions**

335
336 **Fig. 1** BSE images of the condensate blanket adjacent to the laser crater. Panel A
337 provides an overview of the condensate blanket, which can be broken down into well-
338 defined inner and outer zones based on particle morphology. Panel B and C are zoom-in
339 images of Zones 1 – 9 (total length is 300 μm), each section representing approximately

1
2
3 340 40 μm x 35 μm and progressing away from the ablation site. The red dashed square in the
4
5 341 left panel denotes the 250 x 250 micron area for ToF-SIMS imaging.
6
7

8
9 342
10 343 **Fig. 2** Control BSE image of a polished section of the same NIST 610 sample after laser
11
12 344 ablation, but located far (~ 5 mm) away from the ablation site. Note the reduced
13
14 345 distribution of small particle condensates compared to those seen in the outer zone of the
15
16 346 condensation blanket (Fig. 1C, Zones 8 – 9).
17
18

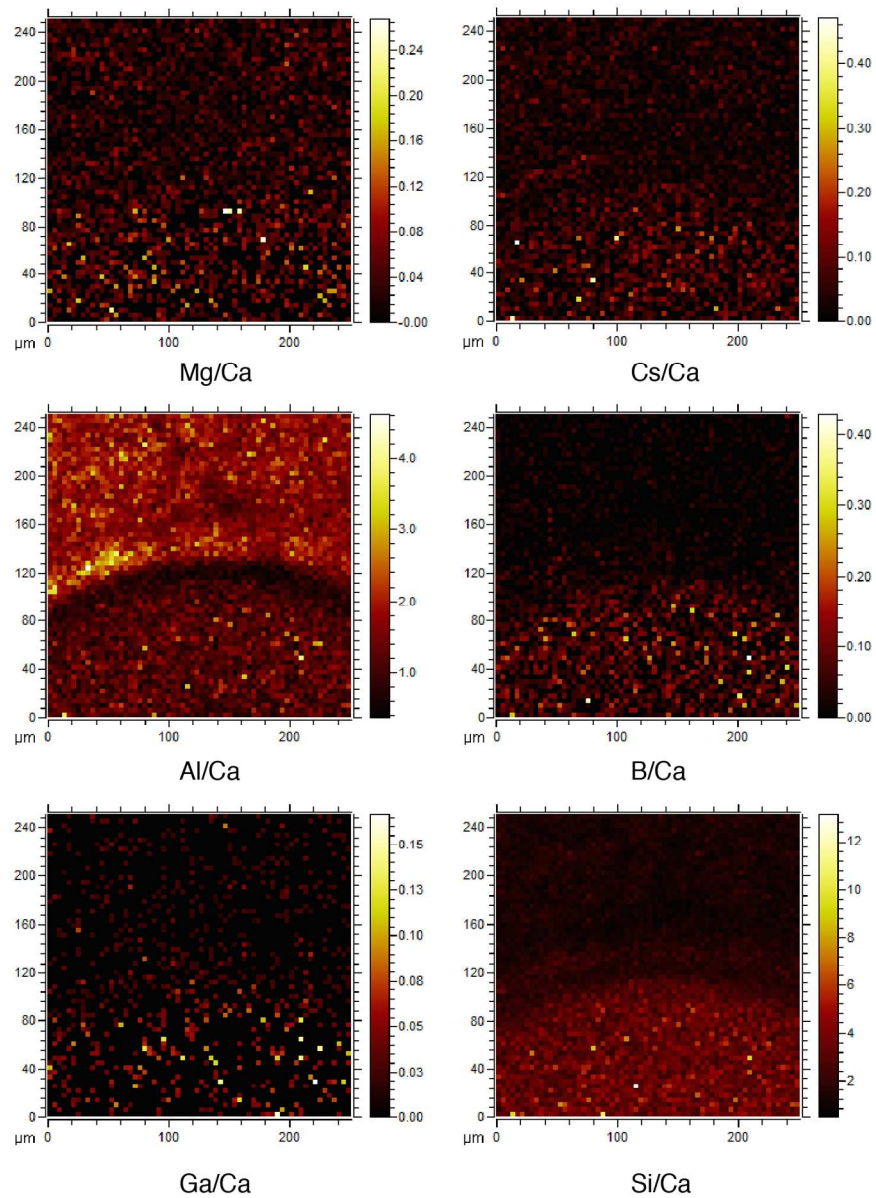
19
20 347
21 348 **Fig. 3** Ca normalized Mg, Cs, Al, B, Ga and Si distributions across the condensate
22
23 349 blanket (first integrated scan). Thermal scale reflects relative ion intensity from low
24
25 350 (black) to high (white)
26
27

28
29 351
30 352 **Fig. 4** Depth profiles of Mg, Cs, Al, B, Ga and Si, all normalized to Ca. A larger scan
31
32 353 number on the x-axis corresponds to a deeper integrated scan. Note the dual y-axes in the
33
34 354 uppermost plots. The gray dots represent the average X/Ca of the 100 μm outermost area
35
36 355 (outer zone), the black dots the average X/Ca of the 100 μm innermost area (inner zone,
37
38 356 nearest the ablation site), and the open circles represent the scan of a far area on the same
39
40 357 NIST 610 glass after ablation. For each X/Ca panel, the $\text{diff}\%$ inner_outer is calculated as
41
42 358 $(X/\text{Ca}_{\text{inner}} - X/\text{Ca}_{\text{outer}}) / [(X/\text{Ca}_{\text{inner}} + X/\text{Ca}_{\text{outer}})/2] * 100\%$. Error bars are $2 \sigma_m$. See text for
43
44 359 more explanation.
45
46
47
48
49

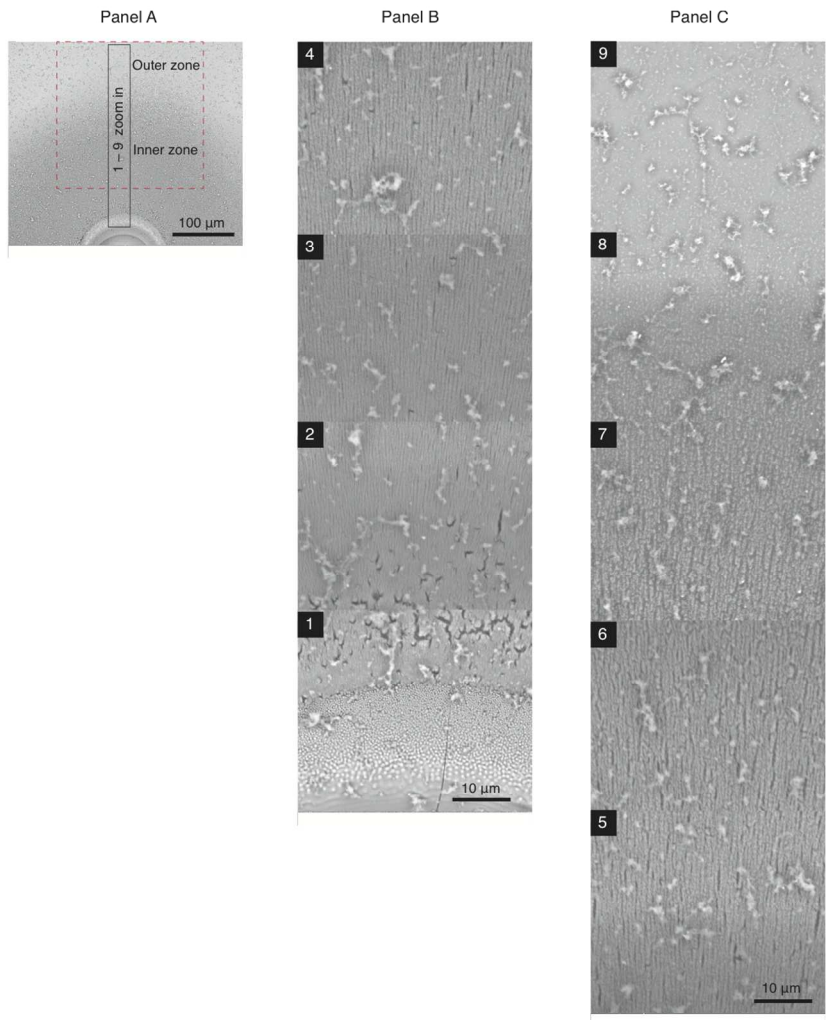
50 360
51 361 **Fig. 5** Average X/Ca $\text{diff}\%$ between the inner and outer zonings. Negative values indicate
52
53 362 relative enrichments in the outer zoning. Elements are defined as volatile, transitional or
54
55 363 refractory based on condensation temperatures derived from Lodders (2003); note that
56
57
58
59
60

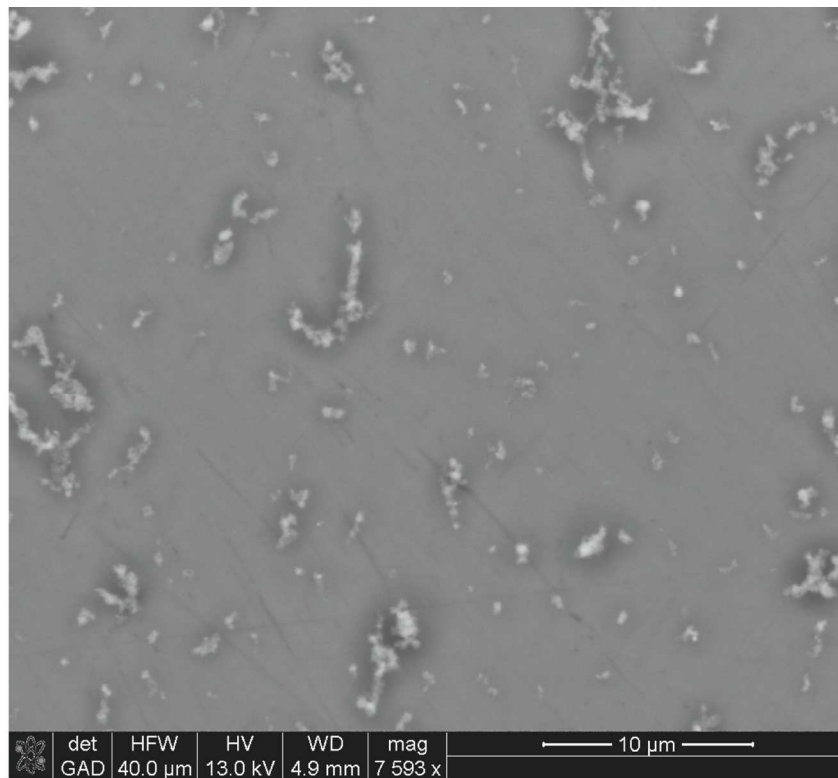
1
2
3 364 these condensation temperatures are determined for a hydrogen atmosphere, while laser
4
5
6 365 ablation was conducted in a helium atmosphere. Errors are $2 \sigma_m$.
7
8

9 366
10 367 **Fig. 6** Average X/Ca diff^o% between the inner and outer zones for alkaline and alkaline
11
12 368 earth metal elements as a function of first ionization potential. Error bars are 2σ , and
13
14 369 some are smaller than the markers.
15
16
17
18
19
20
21
22
23
24
25
26
27
28
29
30
31
32
33
34
35
36
37
38
39
40
41
42
43
44
45
46
47
48
49
50
51
52
53
54
55
56
57
58
59
60

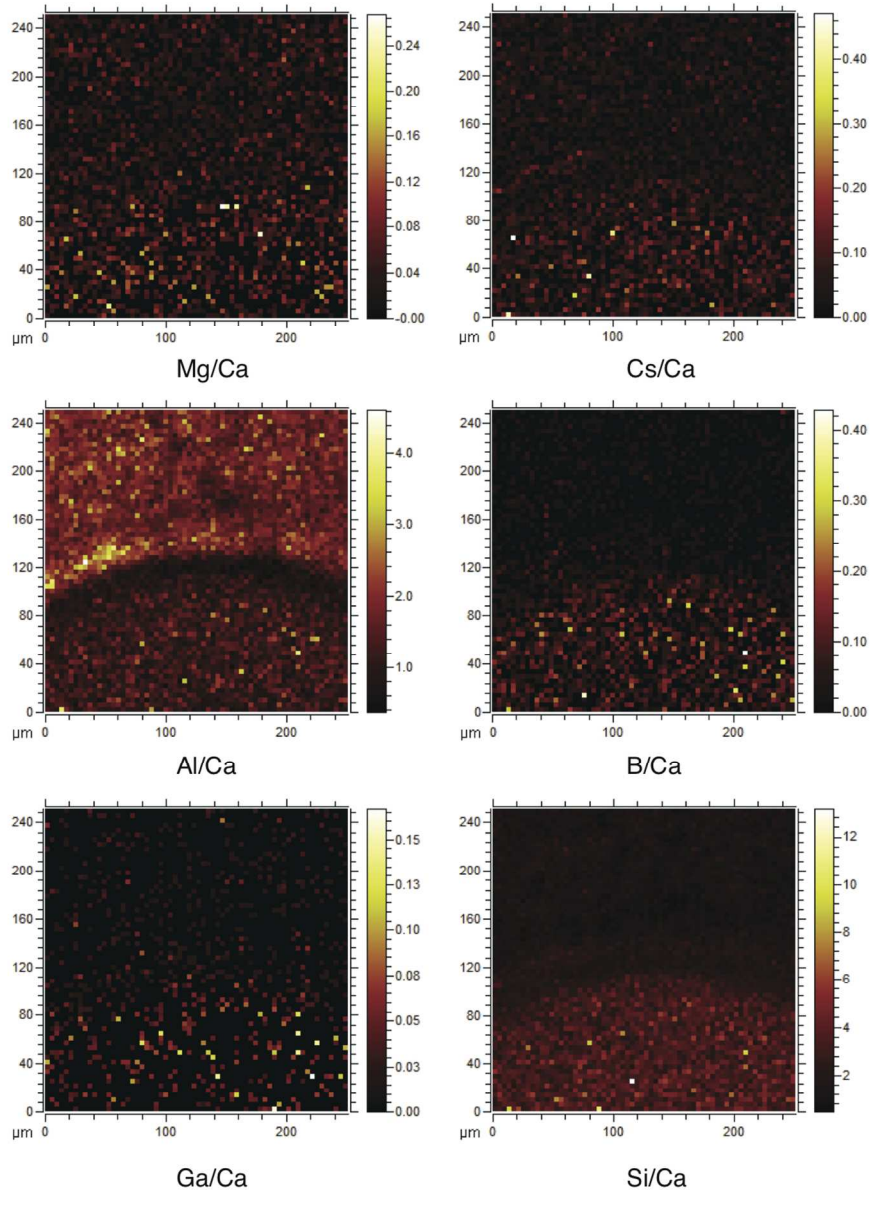
1
2
3
4
5
6
7
8
9
10
11
12
13
14
15
16
17
18
19
20
21
22
23
24
25
26
27
28
29
30
31
32
33
34
35
36
37
38
39
40
41
42
43
44
45
46
47
48
49
50
51
52
53
54
55
56
57
58
59
60

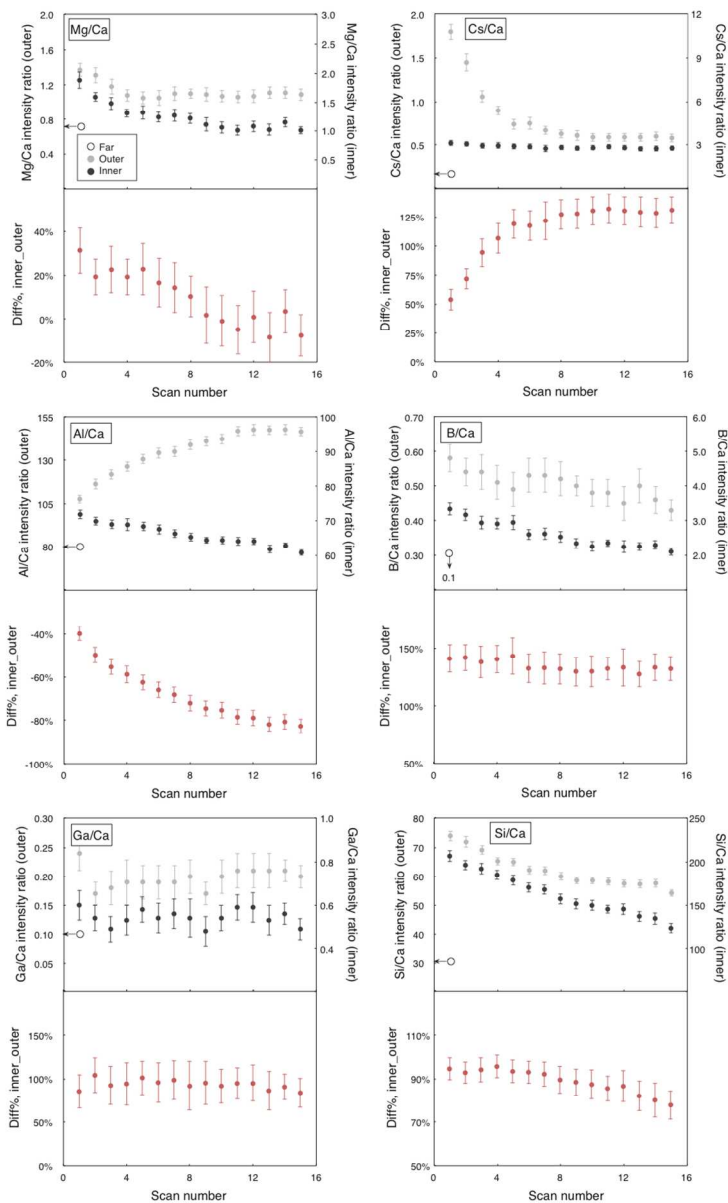
1
2
3
4
5
6
7
8
9
10
11
12
13
14
15
16
17
18
19
20
21
22
23
24
25
26
27
28
29
30
31
32
33
34
35
36
37
38
39
40
41
42
43
44
45
46
47
48
49
50
51
52
53
54
55
56
57
58
59
60

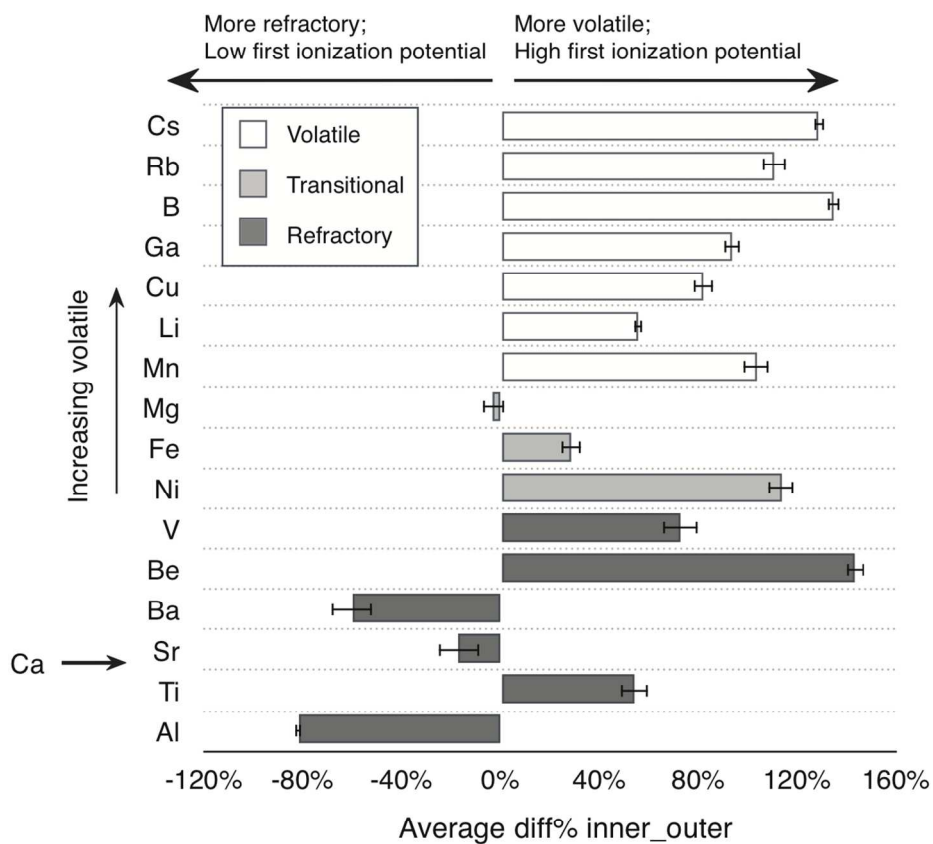




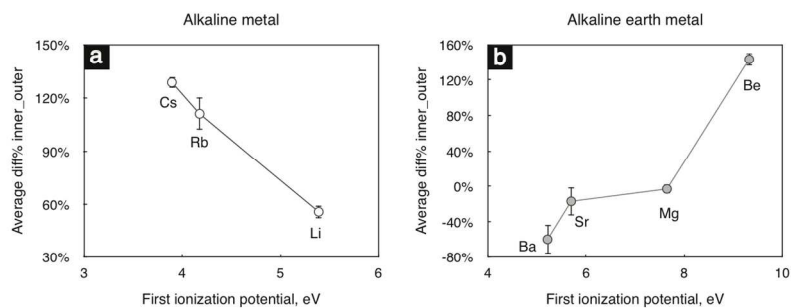
1
2
3
4
5
6
7
8
9
10
11
12
13
14
15
16
17
18
19
20
21
22
23
24
25
26
27
28
29
30
31
32
33
34
35
36
37
38
39
40
41
42
43
44
45
46
47
48
49
50
51
52
53
54
55
56
57
58
59
60



1
2
3
4
5
6
7
8
9
10
11
12
13
14
15
16
17
18
19
20
21
22
23
24
25
26
27
28
29
30
31
32
33
34
35
36
37
38
39
40
41
42
43
44
45
46
47
48
49
50
51
52
53
54
55
56
57
58
59
60



1
2
3
4
5
6
7
8
9
10
11
12
13
14
15
16
17
18
19
20
21
22
23
24
25
26
27
28
29
30
31
32
33
34
35
36
37
38
39
40
41
42
43
44
45
46
47
48
49
50
51
52
53
54
55
56
57
58
59
60

1
2
3
4
5
6
7
8
9
10
11
12
13
14
15
16
17
18
19
20
21
22
23
24
25
26
27
28
29
30
31
32
33
34
35
36
37
38
39
40
41
42
43
44
45
46
47
48
49
50
51
52
53
54
55
56
57
58
59
60